bioRxiv preprint doi: https://doi.org/10.1101/298752; this version posted April 11, 2018. The copyright holder for this preprint (which was not certified by peer review) is the author/funder, who has granted bioRxiv a license to display the preprint in perpetuity. It is made available under aCC-BY-NC-ND 4.0 International license.

Model testing for distinctive functional connectivity gradients with resting-state fMRI data

Jonathan F. O'Rawe[a], Jaime S. Ide[b], and Hoi-Chung Leung[a]

[a]Integrative Neuroscience Program, Department of Psychology, Stony Brook University, Stony Brook, NY, 11794-2500, USA

[b]Department of Psychiatry, Yale University School of Medicine, New Haven, CT, 06519, USA

bioRxiv preprint doi: https://doi.org/10.1101/298752; this version posted April 11, 2018. The copyright holder for this preprint (which was not certified by peer review) is the author/funder, who has granted bioRxiv a license to display the preprint in perpetuity. It is made available under aCC-BY-NC-ND 4.0 International license.

Abstract

In accordance with the concept of topographic organization of neuroanatomical structures, there is an increased interest in estimating and delineating continuous changes in the functional connectivity pattern of neighboring voxels across a region using resting-state fMRI data. Fundamental to this topographic connectivity estimation is the assumption that the organizational gradient is stable across the region of interest. If, however, the region of investigation is actually comprised of multiple subdivisions with different gradients, these estimations would be misleading. Here, we present a model testing procedure to arbitrate between overlapping, shifted, or different topographic connectivity gradients across subdivisions of a structure. We found that this model selection procedure performed well in control conditions of checkerboard subdivisions, which are spatially overlapping subsamples of a region, demonstrating support for overlapping gradients. We then applied the procedure to the striatum, a subcortical structure consisting of the caudate nucleus and putamen, in which an extensive literature suggest to have a shared topographic organization of a diagonal gradient. We found, across multiple resting state fMRI data samples of different spatial resolutions in humans, and one macaque resting state fMRI data sample, that the model with different connectivity gradients across the caudate and putamen was preferred across all data samples. More specifically, within the caudate, we replicated the diagonal organization, but also revealed a medial-lateral organization. Clustering of the putamen only revealed the diagonal gradient. These findings demonstrate the importance of testing basic assumptions even in the case of strong literature support. Indeed, preforming the same analysis assuming a unitary gradient obfuscates the medial-lateral organization of the caudate. Further studies are needed to determine the importance of differential connection gradients across the putamen and caudate and the medial-lateral gradient of the caudate in humans.

Keywords: functional gradient, resting-state fMRI, striatal organization

bioRxiv preprint doi: https://doi.org/10.1101/298752; this version posted April 11, 2018. The copyright holder for this preprint (which was not certified by peer review) is the author/funder, who has granted bioRxiv a license to display the preprint in perpetuity. It is made available under aCC-BY-NC-ND 4.0 International license.

Introduction

A fundamental goal in cognitive neuroscience is characterizing the functional organization of a region (e.g. prefrontal cortex, striatum). In functional neuroimaging, global organization is often examined with the conventional parcellation approach, where signal from a single determined parcel is averaged across the voxels within that parcel and correlated to voxels in the rest of the brain (e.g. Choi, Yeo, & Buckner, 2012), developed in accordance to the topographic nature of region-to-region connections (Kaas, 1997). To study the functional organization of a particular structure with resting state fMRI data, previous studies have utilized a seed based approach and examined the functional connectivity pattern of a structure by separating it evenly or using a number of small seeds distributed across the structure (e.g. Manza et al., 2015). In contrast, recent approaches have started attempting to estimate continuous changes in functional connectivity patterns across the voxels within a parcel. We call this latter approach spatially continuous functional connectivity mapping or functional gradient mapping. Despite the theoretical significance (Jbabdi, Sotiropoulos, & Behrens, 2013; Patel, Kaplan, & Snyder, 2014; Thivierge & Marcus, 2007), the first attempts to directly estimate the functional connectivity gradients using resting-state fMRI data were relatively recent (Haak, Marquand, & Beckmann, 2017; Margulies et al., 2016). In particular, Haak et al.'s (2017) method attempts to infer the gradient maps or connection topographies of a parcel (e.g. motor cortex) by computing the similarity matrix between connectivity fingerprints of all voxels within the parcel and performing spatial statistics across the manifolds of the similarity matrix. However, one fundamental assumption within this method, and any method attempting to resolve connectivity gradients within a parcel, is that there are no sharp shifts in topographic gradients within the parcel under investigation, i.e. the parcel only has spatially contiguous gradients. This assumption is problematic, especially for structures that have known subdivisions of different anatomical connections (e.g. thalamus, striatum).

bioRxiv preprint doi: https://doi.org/10.1101/298752; this version posted April 11, 2018. The copyright holder for this preprint (which was not certified by peer review) is the author/funder, who has granted bioRxiv a license to display the preprint in perpetuity. It is made available under aCC-BY-NC-ND 4.0 International license.

Here we use the striatum as the parcel of interest to describe a set of testing procedures to examine this unitary-gradient assumption. The organization of the striatum, based on rigorous tract tracing studies in the nonhuman primate brain (Haber, 2003; Haber, Fudge, & McFarland, 2000) is suggested to follow a diagonal gradient from dorsolateral to ventromedial, across the entire posterior-to-anterior striatum; this striatal gradient includes both the caudate nucleus and putamen, with the internal capsule considered moreover an arbitrary division between what is otherwise a single nucleus rather than two anatomical regions. Ventromedial portions of the striatum receives projections from orbitofrontal and ventromedial frontal cortex, with the projections from the frontal cortex becoming progressively closer to motor cortex dorsolaterally though the striatum. With this presumed anatomical basis, the functional connectivity gradient of the striatum was examined as a whole in an elegant analysis of resting-state fMRI data (Marquand, Haak, & Beckmann, 2017). Marquand and colleagues (2017) demonstrated the diagonal organization in the human brain and showed that the integrity of this gradient is associated with individual differences in flexible behavior. Their findings provide further support for the diagonal organization which has provided insight into the integration of information as required for new learning (Bar-Gad & Bergman, 2001), as well as the development of deficits in progressive diseases such as Parkinson's Disease, where motor and cognitive symptoms can be predicted by dopamine deficiencies along the anatomical gradient of the striatum (Jokinen et al., 2013; Kish, Shannak, & Hornykiewicz, 1988). However, despite the positive evidence that suggests a single functional connectivity gradient across the striatum as a whole, and the utility of doing so, the assumption of a unitary functional gradient across the striatum remains to be tested.

Here we conducted a set of linear statistical models that can be easily applied to many approaches that attempt to derive or test functional gradient organizations across anatomical space. We apply these models to the striatum to demonstrate their practical utility due to the relatively well-studied striatal anatomy in nonhuman primates, replicating the same results across different human

bioRxiv preprint doi: https://doi.org/10.1101/298752; this version posted April 11, 2018. The copyright holder for this preprint (which was not certified by peer review) is the author/funder, who has granted bioRxiv a license to display the preprint in perpetuity. It is made available under aCC-BY-NC-ND 4.0 International license.

resting-state fMRI samples and across species. These linear statistical models suggested the best evidence for multiple differentiable gradients within each subdivision of the striatum, the caudate nucleus and putamen, instead of a single gradient across the two nuclei.

Methods

Data samples

We utilized data from 4 separate resting-state data samples: the Cambridge Buckner subset of the 1000 functional connectomes, NKI/Rockland data sample, Rockland Enhanced data sample, and Croxson Phillips subset of PRIME-DE. The first three are resting-state fMRI data from human participants, and the fourth is from monkeys. The Cambridge Buckner and NKI/Rockland data samples represent traditional resting-state fMRI protocols, and so the main analyses were run in Cambridge Buckner and initially replicated in NKI/Rockland. The Rockland Enhanced data sample represents a newer resting-state fMRI protocol collected at a higher spatial resolution (2mm isotropic) with the aid of multi-band acceleration. Due to various differences in the data and legacy processed data, some of the data samples were processed in slightly different ways as described below.

For the Cambridge Buckner data sample there were a total of 198 human subjects (123 female from the 1000 Connectomes Project (Biswal et al., 2010) (http://fcon_1000.projects.nitrc.org), ages 18-30 (M = 21.03, SD = 2.31). For the NKI/Rockland data sample (http://fcon_1000.projects.nitrc.org/indi/pro/nki.html), there were a total of 207 human subjects (87 female), ages 4-85 (M = 35.00, SD = 20.00). For the Enhanced Rockland data sample, we used the first 377 human subjects (238 female), ages 8-85 (M = 42.11, SD = 20.34). With the Croxson Phillips data sample, there were 9 monkey subjects, but only 6 (5 Macaca mulatta, 1 Macaca fascicularis) with resting state fMRI data (1 female), ages 3.7-8.0 (M = 5.05, SD = 1.56). All datasets from the Cambridge Buckner database passed the screening for motion other image artifacts (with at least 2/3 usable data per subject after exclusion for FD and DVARS, see below), 18 subjects were excluded from

bioRxiv preprint doi: https://doi.org/10.1101/298752; this version posted April 11, 2018. The copyright holder for this preprint (which was not certified by peer review) is the author/funder, who has granted bioRxiv a license to display the preprint in perpetuity. It is made available under aCC-BY-NC-ND 4.0 International license.

the NKI/Rockland database, leaving 189 subjects (78 female) remaining, ages 4-85 (M = 35.70, SD = 19.89), 78 subjects were excluded from the Rockland Enhanced databased, leaving 299 subjects (194 female), ages 8-85 (M = 40.96, SD = 20.33), all 6 monkeys with resting state data passed motion artifact screening.

MRI Acquisition Parameters

Cambridge Buckner subset (Siemens 3T Trim Trio): T1-weighted images were collected with MPRAGE with the following image parameters: slices = 192, matrix size = 144 x 192, voxel resolution = 1.20 x 1.00 x 1.33 mm^3. Resting state fMRI data were T2*-weighted images acquired using EPI with the following parameters: 47 interleaved axial slices, TR = 3000 ms, voxel resolution = 3.0 x 3.0 x 3.0 mm^3 (119 volumes in total).

NKI/Rockland data (Siemens 3T Trim Trio): T1-weighted images were collected using MPRAGE with the following parameters: slices = 192, matrix size = 256 x 256, resolution = 1.00 x 1.0 x 1.0 mm^3. Resting state fMRI were acquired with the following parameters: 38 interleaved axial slices, slice gap = 0.33 mm, TR = 2500 ms, TE = 30 ms, Flip Angle = 80 deg**,** voxel resolution = 3.0 x 3.0 x 3.0 mm^3 (260 volumes in total).

Enhanced Rockland (Siemens 3T Trim Trio): T1-weighted images were collected using MPRAGE with the following parameters: slices = 176, matrix size = 250 x 250, resolution = 1.00 x 1.0 x 1.0 mm^3. Resting state fMRI data were acquired with the following parameters: Multi-band Acceleration Factor = 4, 64 interleaved axial slices, slice gap = 0 mm, TR = 1400 ms, TE = 30 ms, Flip Angle = 65 deg**,** voxel resolution = 2.0 x 2.0 x 2.0 mm^3 (404 volumes in total).

Croxson Phillips (Philips Achieva 3T): 3 T1-weighted scans were collected with the following parameters: slices = 176, matrix size = 250 x 250, resolution = 0.5 x 0.5 x 0.5 mm^3. Resting state fMRI data were acquired with the following parameters: 40 interleaved axial slices, TR = 2600 ms, TE = 19 ms**,** voxel resolution = 1.5 x 1.5 x 1.5 mm^3 (988 volumes in total).

bioRxiv preprint doi: https://doi.org/10.1101/298752; this version posted April 11, 2018. The copyright holder for this preprint (which was not certified by peer review) is the author/funder, who has granted bioRxiv a license to display the preprint in perpetuity. It is made available under aCC-BY-NC-ND 4.0 International license.

Image Preprocessing

Prior to analysis images were preprocessed utilizing SPM12 (http://www.fil.ion.ucl.ac.uk/spm/software/spm12/). For each individual in the Cambridge Buckner and NKI/Rockland data samples, the functional images were first corrected for slice timing, and then realigned to the middle volume according to a 6 parameter rigid body transformation. Structural images were coregistered with the mean functional image, segmented, and then normalized to the MNI template using both linear and nonlinear transformations. Functional images were then normalized utilizing the same parameters as the structural normalization. For Rockland Enhanced, the functional images were also unwarped during realignment to reduce movement related distortions in the data. For the Croxson macaque data, the three T1 volumes were averaged prior to segmentation to increase SNR, and because fieldmaps were available for all macaques, fieldmap correction was applied to the data prior to slice timing correction to reduce distortions, unwarping was performed during realignment, and data were normalized using the NMT macaque template (Seidlitz et al., 2017).

Further preprocessing steps were performed following the standard procedures of resting-state fMRI analysis either using CONN (Whitfield-Gabrieli & Nieto-Castanon, 2012) or custom Matlab scripts. A nuisance regression was constructed with the following confounding variables: 6 motion parameters up to their second derivatives, scans with evidence of excessive motion (FD > .5 | DVARS > 5), effects of session onset, modeled physiological signal generated through aCompCor (Behzadi, Restom, Liau, & Liu, 2007*)* of the white matter and CSF voxels, and a linear drift component. The residuals of this regression were then filtered utilizing a bandpass between the frequencies of 0.008 and 0.09 Hz and despiked.

For the macaque data, after the data cleaning procedure, each dataset was split into 5-min time bins, and analyses were run on both the full time-series and each time bin.

Spatial Gradient Estimation

bioRxiv preprint doi: https://doi.org/10.1101/298752; this version posted April 11, 2018. The copyright holder for this preprint (which was not certified by peer review) is the author/funder, who has granted bioRxiv a license to display the preprint in perpetuity. It is made available under aCC-BY-NC-ND 4.0 International license.

An atlas based mask of the striatum, including both the caudate and putamen as two subdivisions, was aligned and resampled to the space of each data sample; AAL (Tzourio-Mazoyer et al., 2002) for humans and D99 for macaques (Reveley et al., 2017) (Fig. 1 top). The cleaned time-series from each voxel within the entire striatum was extracted and all pairs of correlations were computed, producing a voxel-voxel correlation matrix **R**. While previous methods utilize the similarity matrix generated from a voxelwise fingerprint (Haak et al., 2017), for simplicity of computation and interpretation we used the direct time-series correlation between each voxel within the striatum. We find these two methods to approximate each other at high numbers of voxels in the brain (see Fig. S1 for simulations and empirical support).

We then calculated a distance matrix as the complement of the correlation matrix, 1-**R**, such that two voxels with perfect correlation are represented with the minimum distance of 0, and voxels perfectly negatively correlated are represented with a maximum distance of 2. Then, using nonmetric multidimensional scaling (MDS) we constructed a 2-dimensional space that best preserves each voxel's bivariate rank distance, defined as the space that minimizes the stress of the configuration (the root mean squared difference between the rank order of the distance matrix and the estimated rank order of the distances within the constructed dimensions (Kruskal, 1964)), the result of which we refer to as "information space". We chose nonmetric MDS because its small set of free parameters (just the dimensionality of the resultant space, which for consistency with prior literature we set to 2 allowing for the estimation of 2 overlapping gradients across space) and allowance for monotonic nonlinearity in the information space (in comparison to the strict linearity metric MDS). However, for demonstration of consistency with the literature, we also used Laplacian Eigenmaps, which constructs dimensions that reproduce the local distances between connected elements of a graph, similar to spectral clustering (Belkin & Niyogi, 2002), with the parameters: {nearest neighbors parameter k = 12 (determines

bioRxiv preprint doi: https://doi.org/10.1101/298752; this version posted April 11, 2018. The copyright holder for this preprint (which was not certified by peer review) is the author/funder, who has granted bioRxiv a license to display the preprint in perpetuity. It is made available under aCC-BY-NC-ND 4.0 International license.

connectivity), heat kernel parameter t = 1 (determines weight of connectivity)}. We found very similar results to those presented in the main manuscript (Fig. S2).

For the scope of our analyses, a functional connectivity gradient across the striatum or each subdivision is defined as the fit of the anatomical space to this information space.

Model Fitting and Model Selection

To select and fit the appropriate model of the functional connectivity gradients, smooth changes in functional connectivity across the space of the striatum, we applied 3 different multivariate multiple regression models, fitting the anatomical space to the information space (Fig. 1 right). Model 1 (M1) predictors containing just the anatomical space information ([x,y,z], rotated with PCA to preserve the spatial variance and mean centered for each striatal subdivision, such that a shift in gradient isn't encoded by the spatial coordinates themselves):

$$[\hat{i_1}, i_2] = \begin{bmatrix} X \\ Y \\ Z \end{bmatrix} \begin{bmatrix} b_1 \\ b_2 \\ b_3 \end{bmatrix}$$

Model 2 (M2) had an additional ROI categorical variable, allowing for a mean shift the spatial gradient across information space for each subdivision:

$$[\hat{i_1}, i_2] = \begin{bmatrix} X \\ Y \\ Z \\ ROI \end{bmatrix} \begin{bmatrix} b_1 \\ b_2 \\ b_3 \\ b_4 \end{bmatrix}$$

Model 3 (M3) additionally had each interaction between the anatomical space information and the ROI categorical variable, allowing for the gradient the change in slope as well across the subdivisions:

bioRxiv preprint doi: https://doi.org/10.1101/298752; this version posted April 11, 2018. The copyright holder for this preprint (which was not certified by peer review) is the author/funder, who has granted bioRxiv a license to display the preprint in perpetuity. It is made available under aCC-BY-NC-ND 4.0 International license.

$$[\hat{i_1}, i_2] = \begin{bmatrix} X \\ Y \\ Z \\ ROI \\ ROI * X \\ ROI * Y \\ ROI * Z \end{bmatrix} \begin{bmatrix} b_1 \\ b_2 \\ b_3 \\ b_4 \\ b_5 \\ b_6 \\ b_7 \end{bmatrix}$$

See Fig. 2 for a representation of this analysis in a single typical subject, with the anatomical space visualized across information space.

To arbitrate the best fitting model, we used the Bayesian Information Criterion (BIC), kln(n) – 2ln(L), where n is the number of voxels, k is the number of parameters, and L is the maximized likelihood of the model. The BIC provides a rough estimation of the log Bayes Factor, and thus is a convenient substitute for model evidence when priors are unknown or hard to quantify (Kass & Raftery, 1995). This model fitting procedure was done for each subject individually, and the reported values are either average change in BIC across models (ΔBIC) or proportion of the population which minimize BIC for each model.

The model selection procedure allows us to select between among the following three possible connectivity gradients within the data: M1, the striatum contains a single unitary gradient overlapping across caudate nucleus and putamen, M2, the caudate nucleus and putamen contain either a continuation of a single gradient or two parallel gradients (carrying different information in the same direction in space), or M3, the caudate nucleus and putamen contain completely different gradients (see Fig. 3A,3C for striatal parcels). Further, we conducted a series of control analyses to ensure that the model selection procedure was arbitrating the proper models. To do so, we took each ROI and generated checkerboard ROIs for each, generating two subparcels that should produce a single completely overlapping gradient and therefore support M1 (Fig. 3B).

bioRxiv preprint doi: https://doi.org/10.1101/298752; this version posted April 11, 2018. The copyright holder for this preprint (which was not certified by peer review) is the author/funder, who has granted bioRxiv a license to display the preprint in perpetuity. It is made available under aCC-BY-NC-ND 4.0 International license.

Visualization of Gradient Results

In order to visualize the two estimated gradients (labeled primary and secondary) across the striatum, the estimated gradients were projected across space, **Xb** mathematically, and plotted onto each voxel within the striatum. Because each subject could theoretically have a different gradient, and even if it follows the same gradient the sign could be arbitrarily flipped, we clustered the gradients prior to averaging. We applied k-means, selecting the cluster solution (out of cluster solutions 1-10) that maximized the ratio of between cluster distance and within cluster distance (Calinski-Harabasz criterion) (Caliński & Harabasz, 1974) for each striatal subdivision separately. We then averaged each subject's estimated gradient projection within cluster in order to avoid heterogeneous averaging. It should be noted here that the primary and secondary labels are arbitrary, we simply output two estimated gradients and label the first primary and the second secondary; these labels do not denote their significance/variance.

Results

Table 1 shows the model fit results for the three models under consideration across all samples.

Primary Results in Cambridge Buckner and NKI/Rockland Data Samples

For the Cambridge Buckner data sample, the mean ΔBICs for M1-M2, M1-M3, and M2-M3, were 37.61, 45.31, and 7.70 respectively, with M3 of the the lowest average BIC and thus the best fitting model. The proportion of individuals that had M1, M2, and M3 as the winning model were 0.04, 0.35, and 0.61 respectively.

For the NKI/Rockland data sample, the mean ΔBICs for M1-M2, M1-M3, and M2-M3, were 83.46, 99.91, and 16.45 respectively, with M3 of the lowest average BIC and thus the best fitting model. The proportion of individuals that had M1, M2, and M3 as the winning model are 0.02, 0.22, and 0.76 respectively.

bioRxiv preprint doi: https://doi.org/10.1101/298752; this version posted April 11, 2018. The copyright holder for this preprint (which was not certified by peer review) is the author/funder, who has granted bioRxiv a license to display the preprint in perpetuity. It is made available under aCC-BY-NC-ND 4.0 International license.

In sum, model testing resulted with M3 as the best fitting model across subjects in both the Cambridge Buckner and NKI/Rockland data samples, suggesting different gradients for the caudate and putamen subdivisions of the striatum, as opposed to a single continuous gradient (M1).

Checkerboard Control Analyses for Cambridge Buckner and NKI/Rockland Data Samples

Caudate

For the Cambridge Buckner data sample, the mean ΔBICs for M1-M2, M1-M3, and M2-M3, were -3.86, -14.75, and -10.89 respectively, with M1 of the lowest average BIC and thus the best fitting model. The proportion of individuals that had M1, M2, and M3 as the winning model are 0.99, 0.01, and 0.00 respectively.

For the NKI/Rockland data sample, the mean ΔBICs for M1-M2, M1-M3, and M2-M3, were -3.67, -14.25, and -10.38 respectively, with M1 of the lowest average BIC and thus the best fitting model. The proportion of individuals that had M1, M2, and M3 as the winning model are 1.00, 0.00, and 0.00 respectively.

In sum, the model testing with the two checkerboard subparcels of the caudate, within both the Cambridge Buckner and NKI/Rockland data samples, expectedly produce the most support for completely overlapping gradient (M1).

Putamen

For the Cambridge Buckner data sample, the mean ΔBICs for M1-M2, M1-M3, and M2-M3, were -4.06, -15.62, and -11.55 respectively, with M1 of the lowest average BIC and thus the best fitting model. The proportion of individuals that had M1, M2, and M3 as the winning model are 1.00, 0.00, and 0.00 respectively.

For the NKI/Rockland data sample, the mean ΔBICs for M1-M2, M1-M3, and M2-M3, were -4.15, -15.45, and -11.30 respectively, with M1 of the lowest average BIC and thus the best fitting

bioRxiv preprint doi: https://doi.org/10.1101/298752; this version posted April 11, 2018. The copyright holder for this preprint (which was not certified by peer review) is the author/funder, who has granted bioRxiv a license to display the preprint in perpetuity. It is made available under aCC-BY-NC-ND 4.0 International license.

model. The proportion of individuals that had M1, M2, and M3 as the winning model are 1.00, 0.00, and 0.00 respectively.

In sum, the model testing with the two checkerboard subparcels of the putamen, within both the Cambridge Buckner and NKI/Rockland data samples, expectedly produce the most support for completely overlapping gradient (M1).

Replication with high resolution fMRI data: Enhanced Rockland Data Sample

We replicated the model fitting results from the lower resolution data samples presented above with higher resolution resting-state fMRI data from the Enhanced Rockland data sample, 2 mm isotropic voxels. The mean ΔBICs for M1-M2, M1-M3, and M2-M3, were 111.18, 147.33, and 36.15 respectively, with M3 of the lowest average BIC and thus being the best fitting model. The proportion of individuals that had M1, M2, and M3 as the winning model are 0.04, 0.12, and 0.84 respectively. Thus we confirmed Model 3 as the best fitting model in these high resolution data, suggesting different functional gradients within the caudate and putamen subdivisions of the striatum.

Replication Across Species: Croxson Macaque Data Sample

To determine whether the gradient modeling outcome is a species level difference between striatal organization in humans and macaques, we conducted the same model testing procedures in resting-state fMRI data from 6 macaque monkeys. The mean ΔBICs for M1-M2, M1-M3, and M2-M3, were 138.69, 211.70, and 73.02 respectively, with M3 of the lowest average BIC and thus being the best fitting model. The proportion of individual monkeys that had M1, M2, and M3 as the winning model are 0.00, 0.00, and 1.00 respectively. We further tested the model fitting separately in each monkey across the N number of time bins and the proportion winning model by time bin was calculated for each monkey; the means and standard deviations are 0.02 (0.04), 0.02 (0.04), 0.97 (0.05), M1, M2, and M3 respectively.

bioRxiv preprint doi: https://doi.org/10.1101/298752; this version posted April 11, 2018. The copyright holder for this preprint (which was not certified by peer review) is the author/funder, who has granted bioRxiv a license to display the preprint in perpetuity. It is made available under aCC-BY-NC-ND 4.0 International license.

Clustering and Characterization of the Functional Gradients

To visualize the model fitting of the functional gradients within the striatum and its two subdivisions, we projected the estimated gradients for each subject within the Enhanced Rockland data sample onto the voxels within the striatum. The Enhanced Rockland data sample were used here for visualization because of the large number of voxels would make the model estimation more reliable. We clustered the caudate and putamen gradients separately due to the model selection results. Similar clustering results were obtained with the Cambridge Buckner database (not shown). The clustering analysis showed a clear peak in this criterion at k = 4 for the caudate subdivision (Fig. 4). The subjects within a cluster were averaged produce the 4 gradient maps, one per cluster (Fig. 5). The two predominate gradient organizations were medial-lateral and a diagonal(from dorsolateral to ventromedial), with participants having both organizations as the primary and secondary gradient more common than having one single organization as both primary and secondary gradients (Fig. 5B, sum of the main diagonal vs sum of the antidiagonal of the contingency table). The insets shown in Figure 5A display the diagonal gradient in the same fashion as in previous papers (Marquand et al., 2017), which illustrates the similarity of both results.

Figure 6 shows the directions of the gradients across the four clusters described above. As the data were clustered using the caudate data only, the average gradient of the putamen likely was not representative of the true gradients within the putamen. However, if M1, a unitary gradient across both the caudate and putamen, really was a good description of the data then clustering one gradient should lead to the clustering of the other. Averaging, therefore, should produce representative gradients where the gradients in both the caudate and the putamen are in the same direction. This was clearly not the case of the Enhanced Rockland data, as none of the clusters demonstrate gradients along the same axes within both the caudate and putamen (Fig. 6).

bioRxiv preprint doi: https://doi.org/10.1101/298752; this version posted April 11, 2018. The copyright holder for this preprint (which was not certified by peer review) is the author/funder, who has granted bioRxiv a license to display the preprint in perpetuity. It is made available under aCC-BY-NC-ND 4.0 International license.

We repeated the same k-means clustering procedure using the gradients of the putamen. The results a diagonal or dorsolateral-ventromedial gradient as the primary organization (Fig. 7). This was the same even when forced into a cluster solution of 4.

We ran these projections using M1, assuming a stable gradient across both caudate nucleus and putamen subdivisions of the striatum. Clustering based on the caudate gradient, we now found the preferred cluster solution to be k = 2, and forcing k = 4 led to the same conclusion: only the diagonal organization was detected. This suggests that assuming that a region of interest contains a single gradient organization can obscure important organizational features if it actually contains two subregions with different gradients (Fig. S3).

Finally, we performed this projection procedure in the macaque sample, demonstrating some similarities to the human data (Fig. 8). One of the striking similarities is the variance of individual differences, depicted in the figure by plotting each individual monkey's gradients.

Discussion

An assumption of many gradient analyses is that there is a unitary gradient (or several overlapping unitary gradients) across the space of the parcel. In this paper, we presented a model testing procedure for this assumption that should be performed prior to analyses intending to estimate gradients within a parcel. This procedure provides clear direction for the investigator: the simplest case is full support of M1, as the parcel should be able to be treated as a single entity. Support for M2 is the same in the case where the mean shift in gradients is along the slope of the gradient. However, in cases of support for M3, or the case of support for M2 where the mean shift is not along the slope of the gradient, the subparcels must be considered separately in the estimation and examination of their gradients. We demonstrated that even for a case where there is a large empirical literature supporting a single or dominant gradient organization within a structure, the striatum, this assumption seems untenable and perhaps overly simplified.

bioRxiv preprint doi: https://doi.org/10.1101/298752; this version posted April 11, 2018. The copyright holder for this preprint (which was not certified by peer review) is the author/funder, who has granted bioRxiv a license to display the preprint in perpetuity. It is made available under aCC-BY-NC-ND 4.0 International license.

We found that the caudate and the putamen, two parcels of the striatum, demonstrate strong model support for having different gradients instead of a single unitary gradient. This result was replicated across multiple data samples, and across species. While the primary purpose of this paper was to introduce the idea of systematically testing the assumptions of the examination of spatial gradients, this result requires some consideration. The primary support for the unitary gradient across the caudate and putamen comes from rigorous nonhuman primate tracing studies (Haber, 2003). While we demonstrated support for M3 across human and nonhuman primates, it's possible that the gradient differences occur solely due to differences in functional organization, rather that structural organization as shown in the tracing work in nonhuman primates by Haber and colleagues. Secondly, it's also possible that the more exhaustive coverage of MRI uncovered a more subtle difference in organization (e.g. Choi et al., 2012) than the sparse sampling necessary in even the most rigorous of tracing studies. Lastly, the generalized diagonal scheme is possibly a simplification of the overall underlying organization. For a unitary gradient to account for the data, two qualities of the data must be satisfied: the projections must be similar in nature (origin), and they must terminate in the same relative location along each nucleus. Some of the direct evidence cited for this organization counters the plausibility of a single unitary gradient: the sharp reduction in projections from caudal motor areas to the caudate in comparison to the putamen (McFarland & Haber, 2000) and the restriction of extent of DLPFC projections to mostly the rostral putamen while strongly projecting across the entire rostral-caudal axis in the caudate (Selemon & Goldman-Rakic, 1985) provide a simple contradiction to these two necessary qualities of the unitary gradient account.

The overwhelming support for different gradients across the caudate and putamen provides new motivation for investigating the organization of each structure. Interestingly, the second organizational gradient we found within the caudate was a strikingly medial-lateral organization. This organization is well founded within nonhuman primate tracing studies (Selemon & Goldman-Rakic, 1985). Given the

bioRxiv preprint doi: https://doi.org/10.1101/298752; this version posted April 11, 2018. The copyright holder for this preprint (which was not certified by peer review) is the author/funder, who has granted bioRxiv a license to display the preprint in perpetuity. It is made available under aCC-BY-NC-ND 4.0 International license.

delineation of the diagonal organization within humans, and the demonstration of its behavioral relevance, it seems that an important next step is to investigate the relevance of this medial-lateral organization in humans.

It's worth it to note that our general approach to fitting gradients is a bit different than previous studies (Haak et al., 2017). We estimate the change in information across space anatomical space linearly. A intuitive description of the spatial fitting step is an attempt to describe the mapping from the anatomical space to information space. While Haak and colleagues (2017) employ a nonlinear mapping approach (similar to nonlinear warping procedure, like normalization), ours is a simple linear mapping of information space to anatomical space (similar to a rigid body transformation, like coregistration). This approach constrains the possible solutions, and thus it should be noted that nonlinear organizations across space will not be detected by our metric. However, the majority of topologies in neuroscience are described in terms of linear transformations of the space, leaving the approach appropriate for the current application. Indeed, the discovery of the same gradient of organization within the caudate as Marquand et al.'s (2017) (Fig. 5A) further lends credence to the usefulness of this approach.

The striatum as a test case it has provided a clear demonstration of the importance of considering the possibility of multiple gradients and the development of model testing procedures to arbitrate between the possibilities.

bioRxiv preprint doi: https://doi.org/10.1101/298752; this version posted April 11, 2018. The copyright holder for this preprint (which was not certified by peer review) is the author/funder, who has granted bioRxiv a license to display the preprint in perpetuity. It is made available under aCC-BY-NC-ND 4.0 International license.

References

Bar-Gad, I., & Bergman, H. (2001). Stepping out of the box: information processing in the neural networks of the basal ganglia. *Current Opinion in Neurobiology*, *11*(6), 689–695. doi:10.1016/S0959-4388(01)00270-7

Behzadi, Y., Restom, K., Liau, J., & Liu, T. T. (2007). A component based noise correction method (CompCor) for BOLD and perfusion based fMRI. *NeuroImage*, *37*(1), 90–101. doi:10.1016/j.neuroimage.2007.04.042

Belkin, M., & Niyogi, P. (2002). Laplacian Eigenmaps and Spectral Techniques for Embedding and Clustering. In T. G. Dietterich, S. Becker, & Z. Ghahramani (Eds.), *Advances in Neural Information Processing Systems 14* (pp. 585–591). MIT Press. Retrieved from http://papers.nips.cc/paper/1961-laplacian-eigenmaps-and-spectral-techniques-for-embedding-and-clustering.pdf

Caliński, T., & Harabasz, J. (1974). A dendrite method for cluster analysis. *Communications in Statistics*, *3*(1), 1–27. doi:10.1080/03610927408827101

Choi, E. Y., Yeo, B. T. T., & Buckner, R. L. (2012). The organization of the human striatum estimated by intrinsic functional connectivity. *Journal of Neurophysiology*, *108*(8), 2242–2263. doi:10.1152/jn.00270.2012

Desikan, R. S., Ségonne, F., Fischl, B., Quinn, B. T., Dickerson, B. C., Blacker, D., … Killiany, R. J. (2006). An automated labeling system for subdividing the human cerebral cortex on MRI scans into gyral based regions of interest. *NeuroImage*, *31*(3), 968–980. doi:10.1016/j.neuroimage.2006.01.021

Haak, K. V., Marquand, A. F., & Beckmann, C. F. (2017). Connectopic mapping with resting-state fMRI. *NeuroImage*. doi:10.1016/j.neuroimage.2017.06.075

Haber, S. N. (2003). The primate basal ganglia: parallel and integrative networks. *Journal of Chemical Neuroanatomy*, *26*(4), 317–330. doi:10.1016/j.jchemneu.2003.10.003

bioRxiv preprint doi: https://doi.org/10.1101/298752; this version posted April 11, 2018. The copyright holder for this preprint (which was not certified by peer review) is the author/funder, who has granted bioRxiv a license to display the preprint in perpetuity. It is made available under aCC-BY-NC-ND 4.0 International license.

Haber, S. N., Fudge, J. L., & McFarland, N. R. (2000). Striatonigrostriatal Pathways in Primates Form an Ascending Spiral from the Shell to the Dorsolateral Striatum. *Journal of Neuroscience*, *20*(6), 2369–2382.

Jbabdi, S., Sotiropoulos, S. N., & Behrens, T. E. (2013). The topographic connectome. *Current Opinion in Neurobiology*, *23*(2), 207–215. doi:10.1016/j.conb.2012.12.004

Jokinen, P., Karrasch, M., Brück, A., Johansson, J., Bergman, J., & Rinne, J. O. (2013). Cognitive slowing in Parkinson's disease is related to frontostriatal dopaminergic dysfunction. *Journal of the Neurological Sciences*, *329*(1), 23–28. doi:10.1016/j.jns.2013.03.006

Kaas, J. H. (1997). Topographic Maps are Fundamental to Sensory Processing. *Brain Research Bulletin*, *44*(2), 107–112. doi:10.1016/S0361-9230(97)00094-4

Kass, R. E., & Raftery, A. E. (1995). Bayes Factors. *Journal of the American Statistical Association*, *90*(430), 773–795. doi:10.1080/01621459.1995.10476572

Kish, S. J., Shannak, K., & Hornykiewicz, O. (1988). Uneven Pattern of Dopamine Loss in the Striatum of Patients with Idiopathic Parkinson's Disease. *New England Journal of Medicine*, *318*(14), 876–880. doi:10.1056/NEJM198804073181402

Kruskal, J. B. (1964). Nonmetric multidimensional scaling: A numerical method. *Psychometrika*, *29*(2), 115–129. doi:10.1007/BF02289694

Manza, P., Zhang, S., Hu, S., Chao, H. H., Leung, H.-C., & Li, C. R. (2015). The effects of age on resting state functional connectivity of the basal ganglia from young to middle adulthood. *NeuroImage*, *107*, 311–322. doi:10.1016/j.neuroimage.2014.12.016

Margulies, D. S., Ghosh, S. S., Goulas, A., Falkiewicz, M., Huntenburg, J. M., Langs, G., … Smallwood, J. (2016). Situating the default-mode network along a principal gradient of macroscale cortical organization. *Proceedings of the National Academy of Sciences*, *113*(44), 12574–12579. doi:10.1073/pnas.1608282113

Marquand, A. F., Haak, K. V., & Beckmann, C. F. (2017). Functional corticostriatal connection topographies predict goal-directed behaviour in humans. *Nature Human Behaviour*, *1*(8), 0146. doi:10.1038/s41562-017-0146

bioRxiv preprint doi: https://doi.org/10.1101/298752; this version posted April 11, 2018. The copyright holder for this preprint (which was not certified by peer review) is the author/funder, who has granted bioRxiv a license to display the preprint in perpetuity. It is made available under aCC-BY-NC-ND 4.0 International license.

McFarland, N. R., & Haber, S. N. (2000). Convergent Inputs from Thalamic Motor Nuclei and Frontal Cortical Areas to the Dorsal Striatum in the Primate. *Journal of Neuroscience*, *20*(10), 3798–3813.

Patel, G. H., Kaplan, D. M., & Snyder, L. H. (2014). Topographic organization in the brain: searching for general principles. *Trends in Cognitive Sciences*, *18*(7), 351–363. doi:10.1016/j.tics.2014.03.008

Reveley, C., Gruslys, A., Ye, F. Q., Glen, D., Samaha, J., E. Russ, B., … Saleem, K. S. (2017). Three-Dimensional Digital Template Atlas of the Macaque Brain. *Cerebral Cortex*, *27*(9), 4463–4477. doi:10.1093/cercor/bhw248

Seidlitz, J., Sponheim, C., Glen, D., Ye, F. Q., Saleem, K. S., Leopold, D. A., … Messinger, A. (2017). A population MRI brain template and analysis tools for the macaque. *NeuroImage*. doi:10.1016/j.neuroimage.2017.04.063

Selemon, L. D., & Goldman-Rakic, P. S. (1985). Longitudinal topography and interdigitation of corticostriatal projections in the rhesus monkey. *The Journal of Neuroscience*, *5*(3), 776–794.

Thivierge, J.-P., & Marcus, G. F. (2007). The topographic brain: from neural connectivity to cognition. *Trends in Neurosciences*, *30*(6), 251–259. doi:10.1016/j.tins.2007.04.004

Tzourio-Mazoyer, N., Landeau, B., Papathanassiou, D., Crivello, F., Etard, O., Delcroix, N., … Joliot, M. (2002). Automated Anatomical Labeling of Activations in SPM Using a Macroscopic Anatomical Parcellation of the MNI MRI Single-Subject Brain. *NeuroImage*, *15*(1), 273–289. doi:10.1006/nimg.2001.0978

Whitfield-Gabrieli, S., & Nieto-Castanon, A. (2012). Conn: A Functional Connectivity Toolbox for Correlated and Anticorrelated Brain Networks. *Brain Connectivity*, *2*(3), 125–141. doi:10.1089/brain.2012.0073

bioRxiv preprint doi: https://doi.org/10.1101/298752; this version posted April 11, 2018. The copyright holder for this preprint (which was not certified by peer review) is the author/funder, who has granted bioRxiv a license to display the preprint in perpetuity. It is made available under aCC-BY-NC-ND 4.0 International license.

Table 1: Results of model testing procedures

Experiment	$\overline{\Delta BIC}$ (M1-M2) [95% CI]	$\overline{\Delta BIC}$ (M1-M3) [95% CI]	$\overline{\Delta BIC}$ (M2-M3) [95% CI]	Prop. Support for M1	Prop. Support for M2	Prop. Support for M3
Striatal Tests						
Cambridge Buckner (n = 198)	37.61 [32.91, 42.32]	45.31 [39.88,50.74]	7.70 [5.56,9.84]	0.04	0.35	0.61
NKI/Rockland (n = 189)	83.46 [74.25,92.67]	99.91 [89.34,110.48]	16.45 [13.17,19.73]	0.02	0.22	0.76
Rockland Enhanced (n = 299)	111.18 [96.51,125.84]	147.33 [130.29,164.36]	36.15 [31.43,40.86]	0.04	0.12	0.84
Croxson Macaque (n = 6)	138.69 [-41.83,319.20]	211.70 [3.53,419.87]	73.02 [40.48,105.56]	0.00	0.00	1.00
Caudate Checkerboard						
Cambridge Buckner (n = 198)	-3.86 [-3.98,-3.73]	-14.75 [-15.05,-14.45]	-10.89 [-11.16,-10.62]	0.99	0.01	0.00
NKI/Rockland (n = 189)	-3.67 [-3.99,-3.75]	-14.25 [-14.59,-13.91]	-10.38 [-10.69,-10.06]	1.00	0.00	0.00
Putamen Checkerboard						
Cambridge Buckner (n = 198)	-4.06 [-4.17,-3.95]	-15.62 [-15.89,-15.35]	-11.55 [-11.79,-11.32]	1.00	0.00	0.00
NKI/Rockland (n = 189)	-4.15 [-4.25,-4.05]	-15.45 [-15.75,-15.14]	-11.30 [-11.58,-11.02]	1.00	0.00	0.00

bioRxiv preprint doi: https://doi.org/10.1101/298752; this version posted April 11, 2018. The copyright holder for this preprint (which was not certified by peer review) is the author/funder, who has granted bioRxiv a license to display the preprint in perpetuity. It is made available under aCC-BY-NC-ND 4.0 International license.

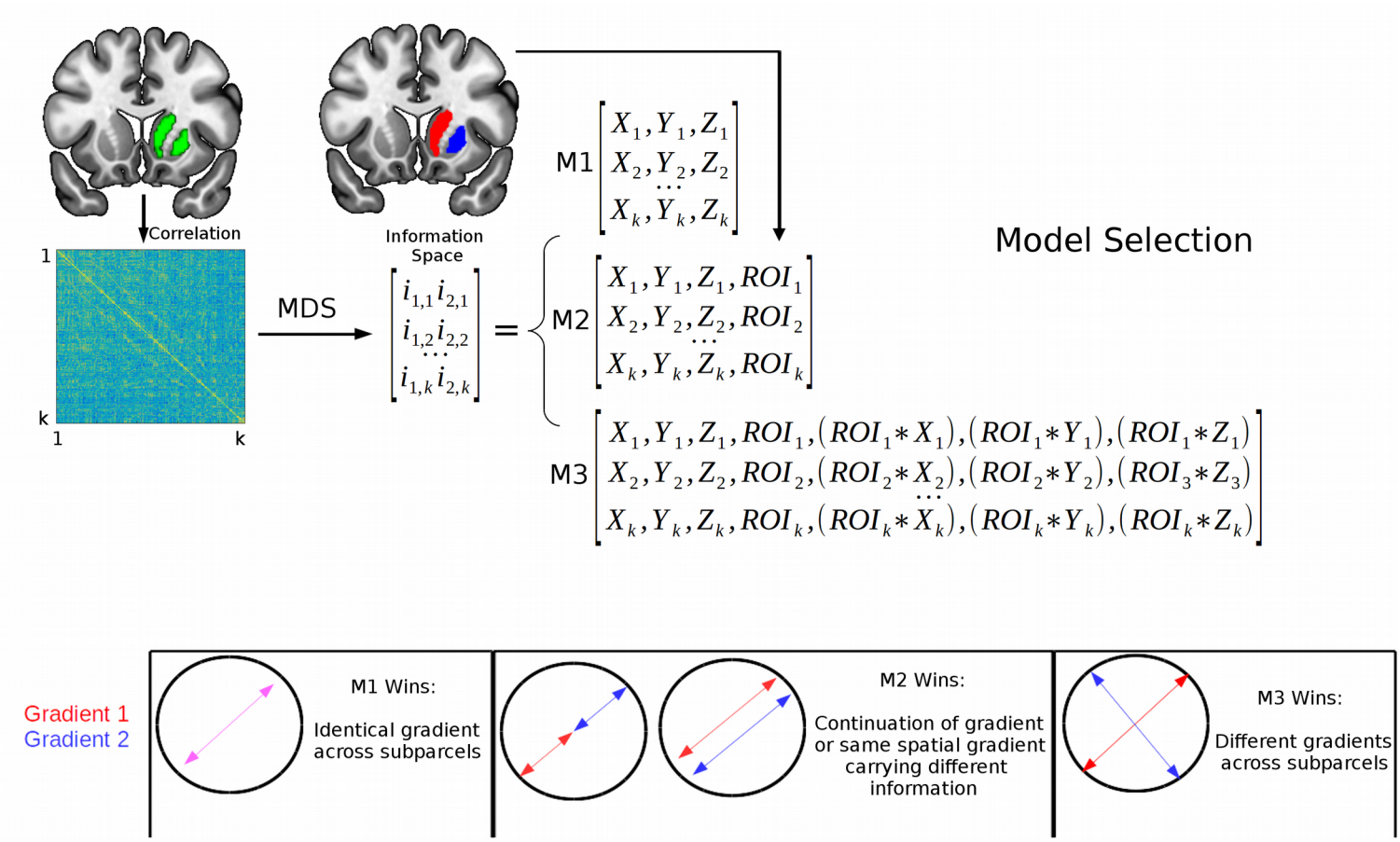

Figure 1: Analysis and Models. The time-series of each voxel within the superparcel (caudate + putamen; top left, green) was extracted, and the correlations between all pairs of voxel time-series were calculated. This produced a k by k correlation matrix, where k is the number of voxels within the superparcel. A distance matrix was computed by taking the complement of this correlation matrix, and this distance matrix is reduced into a two dimensional space using nonclassical mutidimensional scaling (MDS), producing an "information space". To test the three potential gradient models, we then fit this information space with the anatomical space information from the superparcel (i.e. Model 1 [M1]), with Model 2 (M2) including a categorical term (ROI, being within the caudate or the putamen subdivision for each voxel), and Model 3 (M3) also including the interaction between the spatial information and the categorical variable. The bidirectional arrows represent the hypothetical functional gradient(s) within the structure for the case of each winning model.

bioRxiv preprint doi: https://doi.org/10.1101/298752; this version posted April 11, 2018. The copyright holder for this preprint (which was not certified by peer review) is the author/funder, who has granted bioRxiv a license to display the preprint in perpetuity. It is made available under aCC-BY-NC-ND 4.0 International license.

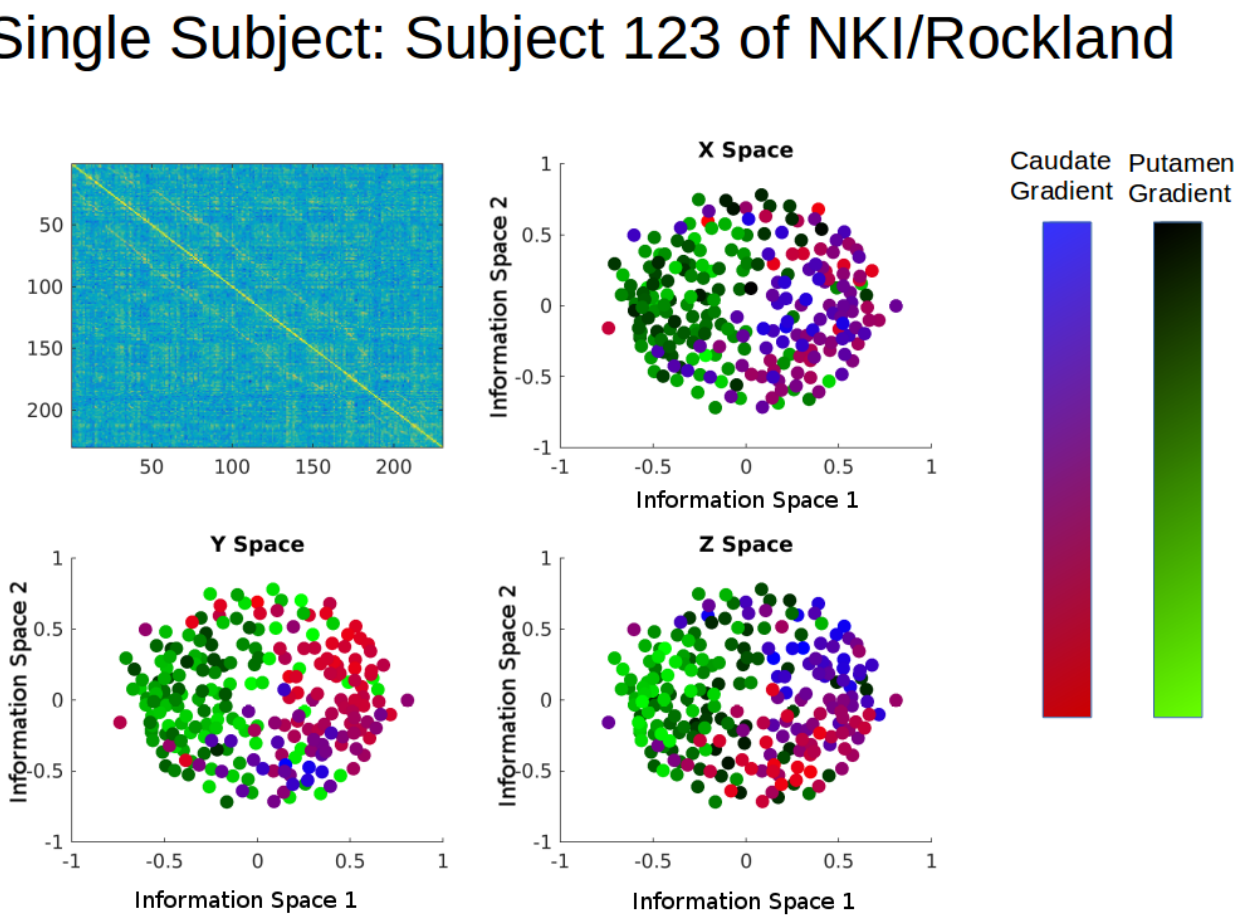

Figure 2: An example subject from the NKI/Rockland database. The top left is the voxel-voxel correlation matrix from which the information dimensions were subsequently derived. The 3 panes show all voxels in their information space, with the anatomical space (X, Y, Z) of each subdivision or ROI (caudate and putamen) represented as a color gradient. A smooth transition of colored dots represents good fit of that anatomical gradient to the information space.

bioRxiv preprint doi: https://doi.org/10.1101/298752; this version posted April 11, 2018. The copyright holder for this preprint (which was not certified by peer review) is the author/funder, who has granted bioRxiv a license to display the preprint in perpetuity. It is made available under aCC-BY-NC-ND 4.0 International license.

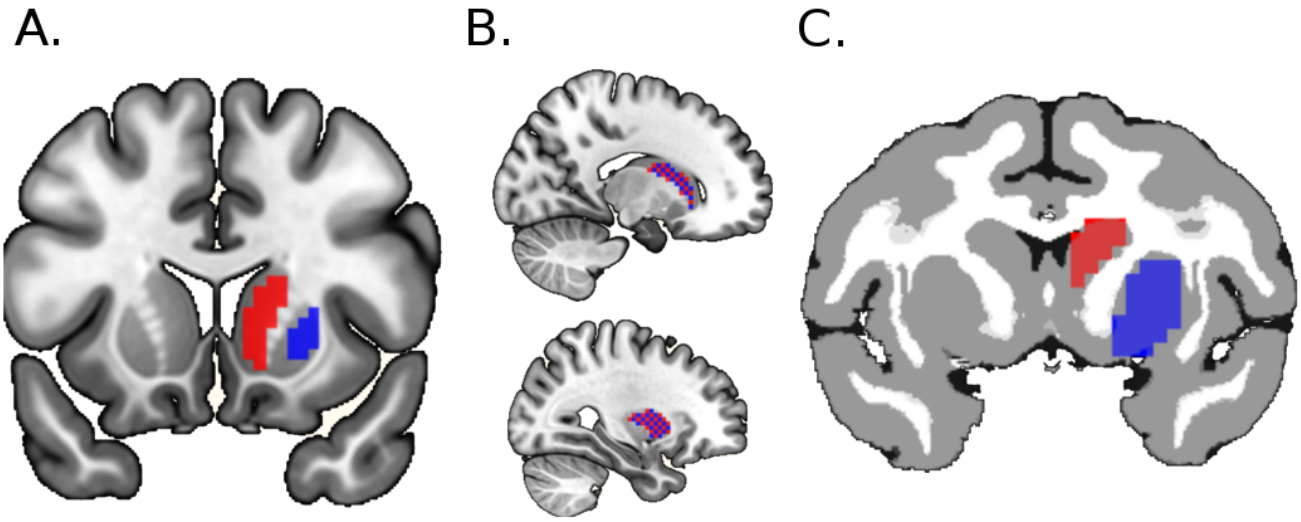

Figure 3: Striatal subdivisions for different model testing procedures. **(A)** For the striatal model testing procedure in humans, the AAL masks for the caudate (red) and putamen (blue) were eroded, the superparcel being defined as the combination of both. **(B)** Caudate (top) and Putamen (bottom) masks for the checkerboard control analyses. **(C)** For the striatal model testing procedure in macaques, the D99 atlas masks for caudate (red) and putamen (blue), with the superparcel being defined as the combination of both.

bioRxiv preprint doi: https://doi.org/10.1101/298752; this version posted April 11, 2018. The copyright holder for this preprint (which was not certified by peer review) is the author/funder, who has granted bioRxiv a license to display the preprint in perpetuity. It is made available under aCC-BY-NC-ND 4.0 International license.

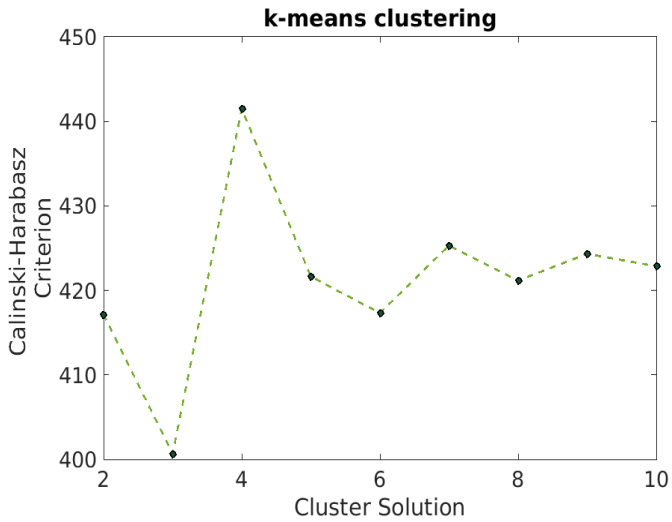

Figure 4: Clustering Solution for the functional gradients of the caudate subdivision. Ratio of between cluster distance and within cluster distance (Calinski-Harabasz criterion) as a function of number of clusters. A clear peak at 4 indicates this as the preferred solution.

bioRxiv preprint doi: https://doi.org/10.1101/298752; this version posted April 11, 2018. The copyright holder for this preprint (which was not certified by peer review) is the author/funder, who has granted bioRxiv a license to display the preprint in perpetuity. It is made available under aCC-BY-NC-ND 4.0 International license.

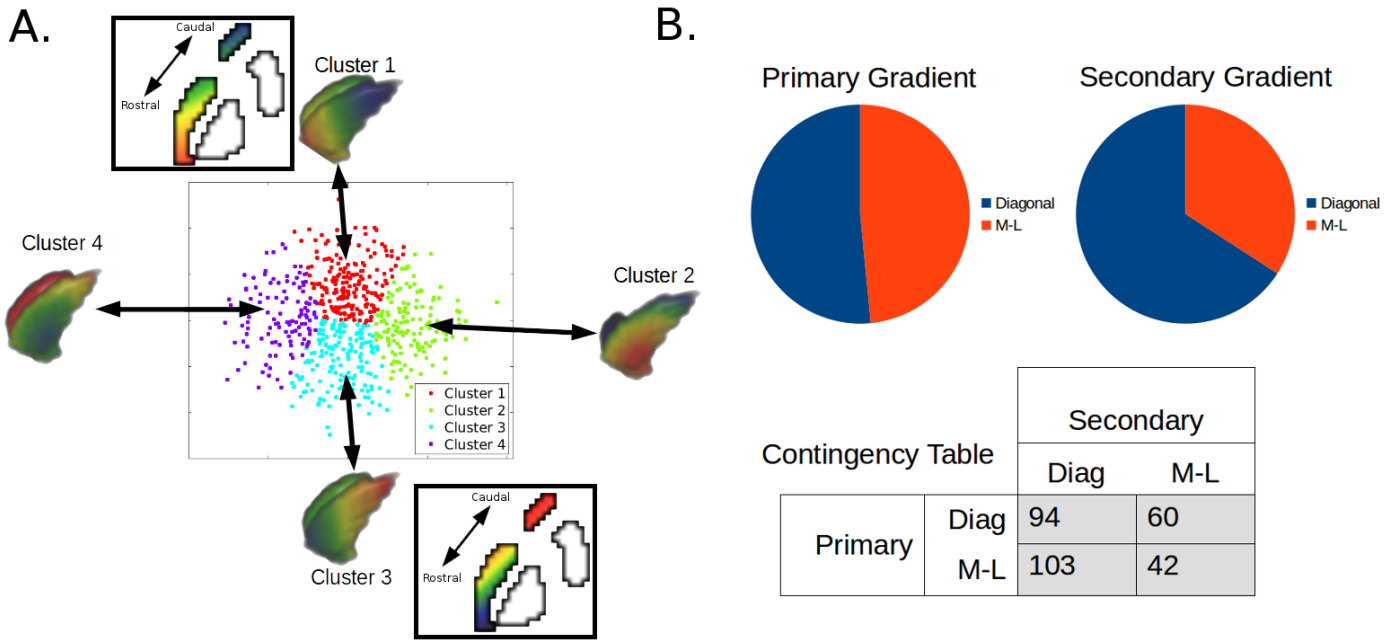

Contingency Table

		Secondary	
		Diag	M-L
Primary	Diag	94	60
	M-L	103	42

Figure 5: Clustering of the gradient results for the caudate. **(A)** K-means clustering was applied to very subject's primary and secondary gradients, visualized by the scatter plot were each dot represents a single subject's primary or secondary gradient. The mean gradient of each cluster is visualized, clusters 1 and 3 representing the flipped versions of the same diagonal gradient, while 2 and 4 represent flipped versions of the same medial-lateral gradient. The insets next to clusters 1 and 3 are representations of each of these gradients visualized in the same formate as the prior literature. This is to show the similarity in the diagonal gradient between our results and Marquand et al.'s (2017) results. **(B)** Top: proportion of subjects displaying each organization within each estimated gradient. Bottom: A contingency table illustrates that displaying both gradients (anti-diagonal) is more common than displaying a single organization across both estimated gradients (main diagonal)

bioRxiv preprint doi: https://doi.org/10.1101/298752; this version posted April 11, 2018. The copyright holder for this preprint (which was not certified by peer review) is the author/funder, who has granted bioRxiv a license to display the preprint in perpetuity. It is made available under aCC-BY-NC-ND 4.0 International license.

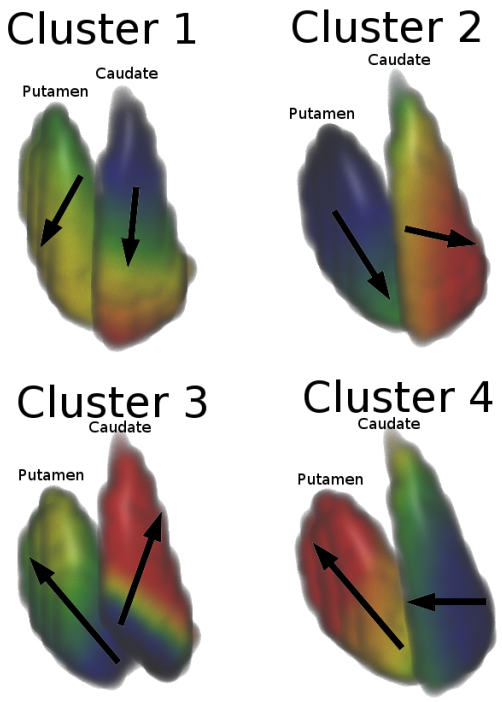

Figure 6: The average caudate and Putamen gradients averaged within clusters based on the caudate gradients. The disagreement in angle of each of the gradients between caudate and putamen act as a visualization for the support of model 3.

bioRxiv preprint doi: https://doi.org/10.1101/298752; this version posted April 11, 2018. The copyright holder for this preprint (which was not certified by peer review) is the author/funder, who has granted bioRxiv a license to display the preprint in perpetuity. It is made available under aCC-BY-NC-ND 4.0 International license.

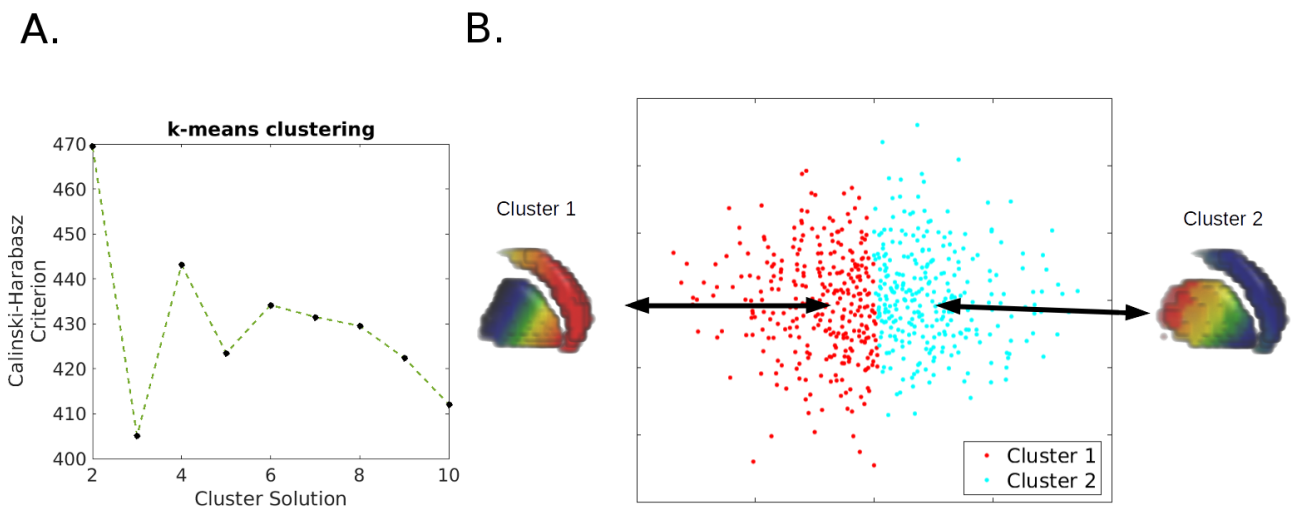

Figure 7: Clustering of the gradient results of the putamen. **(A)** A peak in the ratio of between cluster distance and within cluster distance (Calinski-Harabasz criterion) at k = 2 indicates this as the preferred cluster solution. **(B)** The two cluster solution demonstrates the diagonal gradient as the primary functional gradient for the putamen.

bioRxiv preprint doi: https://doi.org/10.1101/298752; this version posted April 11, 2018. The copyright holder for this preprint (which was not certified by peer review) is the author/funder, who has granted bioRxiv a license to display the preprint in perpetuity. It is made available under aCC-BY-NC-ND 4.0 International license.

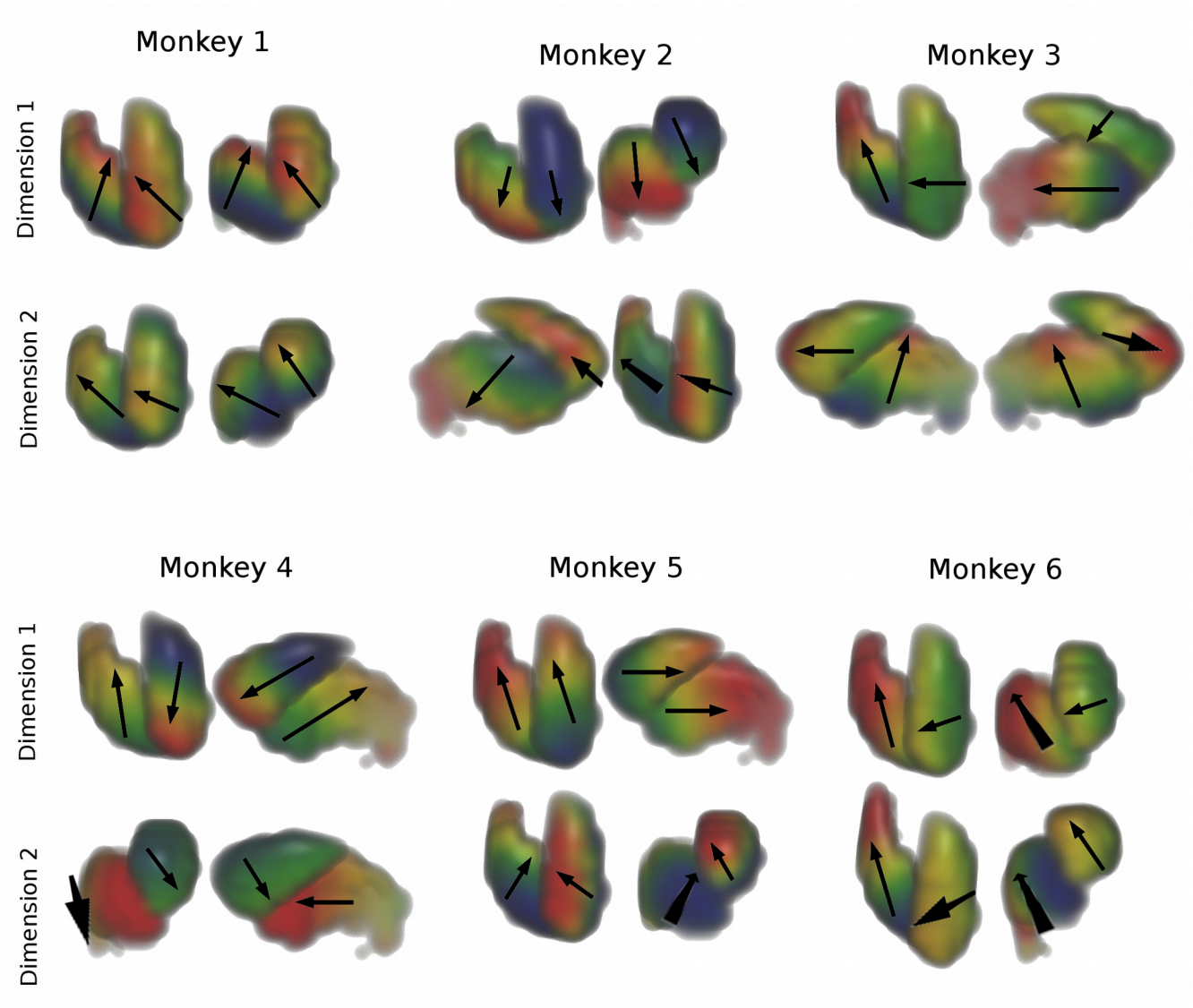

Figure 8: Gradient projection in each individual monkey of the Croxson data sample. The nonhuman primates also showed vast individual differences in functional topology of the striatum, with monkeys demonstrating one or two motifs out of several. With the caudate, these motifs include medial-lateral, diagonal, and anterior-posterior. Consistent with the human modeling results, no monkey demonstrated identical gradients within caudate and putamen across both estimated gradients/information dimensions.